Received August 18, 2021, accepted September 5, 2021, date of publication September 9, 2021,
date of current version September 17, 2021.

Digital Object Identifier 10.1109/ACCESS.2021.3111452

Optimal Shunt-Resonance Fault Current Limiter for Transient Stability Enhancement of a Grid-Connected Hybrid PV/Wind Power System

AHMED M. A. IBRAHIM[1], I. HAMDAN[1], SAAD F. AL-GAHTANI[2], (Member, IEEE), HANY S. HUSSEIN[2,3], (Senior Member, IEEE), LOAI S. NASRAT[3], (Member, IEEE), AND MOHAMED A. ISMEIL[1,4]

[1]Electrical Engineering Department, Faculty of Engineering, South Valley University, Qena 83523, Egypt
[2]Electrical Engineering Department, Faculty of Engineering, King Khalid University, Abha 61411, Saudi Arabia
[3]Electrical Engineering Department, Faculty of Engineering, Aswan University, Aswan 81528, Egypt
[4]APEARC, Faculty of Engineering, Aswan University, Aswan 81528, Egypt

Corresponding author: Mohamed A. Ismeil (mohamedismeil@eng.svu.edu.eg)

This work was supported by the Deanship of Scientific Research, King Khalid University, Abha, Saudi Arabia, through General Research Project, under Grant GRP/66/42.

ABSTRACT This paper proposes an optimal design of Shunt-Resonance Fault Current Limiter (SRFCL) to enhance the Fault Ride-Through (FRT) capability and improve the transient stability of a grid-connected hybrid PV/wind power system. The design parameters of the SRFCL are optimized by using Particle Swarm Optimization (PSO) technique. The proposed SRFCL topology is designed in such a way that it can provide superior protection capability for limiting the fault current and supporting the grid voltage than the conventional Bridge Fault Current Limiter (BFCL). The effectiveness of the SRFCL in supporting the dynamic performance and improving the transient stability of the hybrid energy system is validated during both symmetrical and unsymmetrical faults in the electrical utility. Moreover, its credibility is evaluated compared with that of the BFCL and the FRT control schemes. Simulations have been performed using the MATLAB/SIMULINK software. The results illustrate that the proposed SRFCL augments significantly the dynamic behavior and the transient stability of the hybrid power system during the fault events. Also, when the optimal SRFCL is employed, the injected active power by the hybrid system and the grid voltage profile are improved considerably under the grid disturbances. Furthermore, the comparison confirms the superiority of the SRFCL performance to both the BFCL topology and the FRT control scheme in every aspect.

INDEX TERMS PV, wind, fault ride-through (FRT), bridge fault current limiter (BFCL), shunt-resonance current limiter (SRFCL), particle swarm optimization (PSO).

LIST OF ABBREVIATIONS

BFCL	Bridge Fault Current Limiter.
DFIG	Doubly Fed Induction Generator.
FCL	Fault Current Limiter.
FRT	Fault Ride-Through.
GSC	Grid Side Converter.
PCC	Point of Common Coupling.
PSO	Particle Swarm Optimization.
RSC	Rotor Side Converter.
SRFCL	Shunt-Resonance Fault Current Limiter.
VSI	Voltage Source Inverter.

The associate editor coordinating the review of this manuscript and approving it for publication was Inam Nutkani.

I. INTRODUCTION

Nowadays, the rapid depletion of conventional energy sources and the perpetual rise in demand for electricity as well as the environmental concerns have necessitated devising new techniques to utilize renewable sources as alternative energy sources [1]. Among the renewable energy sources, solar energy and wind energy are becoming the most prominent energy sources to be integrated with the power systems due to their abundant advantages such as high production capability and low maintenance cost. Solar energy is growing so quickly globally and its penetration level is significant currently because of the low cost of PV cells and the developed power electronics technology. Also, wind energy

is considered the most effective and vital renewable energy source today since being global and can be harnessed to generate great electric power with enhanced quality. Moreover, the fast growth of utilizing wind energy is mainly credited to the Doubly Fed Induction Generator (DFIG) technology due to its numerous advantages such as decoupled control of active and reactive power, maximum power extraction, and partial rating converter [2]. Recently, the most popular trend of renewable sources is merging PV and wind energy sources as a PV/wind hybrid power generation system capable of injecting greater power with higher continuity and reliability [3], [4]. The penetration of large-scale hybrid power systems consisting of PV stations and wind farms into the electrical grid has been reported in [5].

Even though the PV/wind hybrid energy systems can offer significant advantages through integration with the electrical utilities, they are very sensitive to grid faults occurrence. Concerning the PV systems, the transient faults cause an imbalance between the generated PV power and the injected power from the inverter into the grid which results in a severe increase of the intermediate DC-link voltage and may damage the power electronic interfaces [6]. The adverse impacts of penetration of large-scale grid-connected PV plants on the power system stability have been detailed discussed in [7]. On the other hand, the DFIG based wind farms are extremely susceptible to grid faults since the DFIG stator windings are directly connected to the network. Thus, in the event of grid fault, the DFIG terminal voltage goes very low, which results in a large current through the stator and rotor windings, DC-link overvoltage, and rotor overspeed that makes the system operation unstable and may damage the machine [8]. According to the new grid codes, all grid-connected renewable energy stations should have the Fault Ride Through (FRT) capability during the transient faults. The FRT implies the power generation plants stay connected to the grid even during fault events and inject simultaneously reactive power to enhance the power system stability [9].

Different topologies have been introduced in literatures to improve the FRT capability of grid-tied power generation systems under network disturbances. Among them, Al-Shetwi *et al.* [10] discussed in detail the advantages and limitations of several FRT capability enhancement approaches employed for the grid-connected PV systems. In [11], the paper presented a comprehensive control strategy to enhance the FRT capability for single-stage inverter-based PV station connected to the Malaysian utility grid. The simulation results illustrated the capability of the control to overcome both the DC-link overvoltage and AC overcurrent problems that may damage the employed inverter. However, despite the effectiveness of the FRT strategy during both symmetrical and unsymmetrical faults, it requires an additional DC-chopper brake controller to absorb the excessive DC-link voltage, and also its performance is highly dependent on the fault detection method. Noureldeen and Ibrahim [12] presented an effective control strategy based on the modification of the control approach and activation of the outer crowbar protection system to enhance the FRT capability of grid-connected large-scale hybrid PV/wind power system. Although the FRT control strategy showed superior performance during the unbalanced faults such as double-line-to-ground (2LG) and line-to-ground (1LG), it incurs some limitations during the three-line-to-ground (3LG) fault.

Furthermore, several works have recommended the employment of FACTS devices to enhance the FRT capability and improve the transient stability of the grid-integrated power generation systems during fault events. Among them, Movahedi *et al.* [13] investigated the effect of three FACTS controllers on the transient stability improvement of a grid-connected large-scale hybrid power system consisting of a 120 MW PV plant and two 200 MW wind farms. Hemeida *et al.* [14] presented a comprehensive comparison for the STATCOM employment versus the SVC to promote the transient stability of wind farm interconnected with a multi-machine power system. The study concerned to improve the system dynamic performance in the post-fault duration and the simulation results confirmed the superior impact of the STATCOM compared with the Static Var Compesnasator (SVC) when subjected to 3LG fault at different locations in the grid. In [15], the paper presented the utilization of STATCOM in reactive power compensation to enhance the dynamic behavior for a grid-tied hybrid PV/wind energy system under the fault events. The results validated the effectiveness of the STATCOM controller in improving the transient stability compared with the conventional FRT control scheme when a severe three-phase grid voltage sag occurs. However, most previous solutions to improve transient stability have emphasized the employment of high rating power electronics which incurs the high-cost problem, while other methods that require modification of the control techniques are more feasible for new integrations.

Recently, the bridge-type fault current limiter (BFCL) with different configurations and limiting impedances have been introduced as a cost-effective strategy to improve the transient stability and enhance the FRT capability of the power system. Hossain [16] introduced a BFCL configuration comprising a series-connected resistor and inductor in parallel with a capacitor to augment the transient stability performance of a grid-connected wind power station. The obtained results showed the effectiveness of the employed BFCL compared with the series dynamic braking resistor (SDBR) and solid-state fault current limiter (SSFCL) during the 3LG and the 1LG faults. In [17], scholars applied Sliding Mode Control (SMC) approach for the BFCL to promote the FRT performance of a DFIG-based wind turbine integrated with the grid. The results revealed that the SMC-based BFCL offers superior performance compared with the conventional PI controller during both symmetrical and unsymmetrical short-circuit faults. Rashid and Ali [18] presented a BFCL topology consisting of an inductor in parallel with a capacitor to improve the FRT capability of a DFIG-based wind farm. The simulation results revealed the superiority of the implemented BFCL over the crowbar protection system during different

fault conditions. In [19], the paper validated the reliability of inductive-capacitive-type BFCL based on neuro-fuzzy logic control than the conventional BFCL and the SDBR in improving the FRT capability of DFIG-based wind farm during the 3LG and 1LG faults. Firouzi *et al.* [20] presented a voltage adaptive BFCL to alleviate the overvoltage of a DFIG connected with a wind power station during voltage sag conditions, where the appropriate resistor of BFCL is inserted according to the voltage drop depth. However, the main drawback of the BFCL is that it offers humble performance under the severe faults in the grid since its impedance becomes less effective for power evacuation during acute disturbances [21].

Motivated by the aforementioned background, this study proposes an optimal SRFCL topology to augment the FRT capability and improve the transient stability of a grid-integrated hybrid PV/wind power system. The hybrid power generation system consists of a 2 MW PV plant integrated with a DFIG-based wind farm of 4 MW through a common AC bus. The proposed SRFCL configuration is designed in such a way that it can offer superior protection capability for limiting the fault current and supporting the grid voltage than the BFCL during the transient faults. Moreover, the main contributions of the paper are summarized as follows:

- An optimal SRFCL protection strategy is proposed to enhance the FRT capability and improve the transient stability of a grid-connected hybrid PV/wind power system.
- The design parameters of the SRFCL are obtained by using the PSO technique
- The effectiveness of the proposed SRFCL is validated compared with the conventional BFCL and the FRT control scheme during both symmetrical and unsymmetrical faults in the electrical grid.
- Also, the performance of the proposed SRFCL is evaluated compared with the previous topologies of the Fault Current Limiter (FCL) suggested in [18], [19].

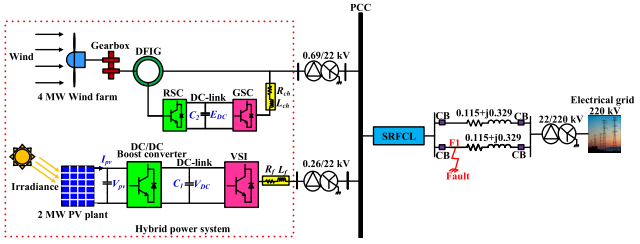

FIGURE 1. Schematic diagram of the PV/wind hybrid system integrated with the SRFCL.

II. POWER SYSTEM MODEL DESCRIPTION

In this work, the hybrid power system model illustrated in Fig. 1 is utilized for dynamic performance and transient stability analysis. It consists of a PV plant of 2 MW integrated with DFIG based wind farm of 4 MW through a common AC bus (22 kV). Also, the SRFCL protection strategy is inserted between the Point of Common Coupling (PCC) and the parallel transmission lines during external grid faults to augment the transient stability and the FRT capability of the hybrid system. In regards to the solar plant, it consists of 1320 parallel-connected strings, each string comprises 5 PV modules linked in series from Sunpower WHT-D type with a maximum power of 305 W. The design specifications of the selected module are summarized in Table 1 and the rest of the parameters are available at [22]. Besides, the solar plant involves a DC/DC boost converter for extracting the peak generated power at varying irradiation and it is interconnected with the PCC via a three-phase Voltage Source Inverter (VSI).

Moreover, the implemented wind farm which possesses a rated power of 4 MW, includes DFIG based Gamesa G80 wind turbine with the technical specifications shown in Table 1. Also, the rest of the employed wind turbine specifications are available in [23]. The DFIG can regulate the generated active and reactive power independently by controlling the Rotor Side Converter (RSC) and the Grid Side Converter (GSC), respectively. The performed control scheme of the DFIG converters is detailed discussed in the following sections.

III. GRID FAULT IMPACTS ON THE HYBRID POWER SYSTEM

This work employed a two-stage grid-tied PV plant as depicted in Fig. 1, the first stage is the DC/DC boost converter while the second stage is the three-phase DC/AC inverter. The PV system has been modeled in MATLAB/SIMULINK software using the equations explained in [24], [25], and also the overall power flow through it can be expressed as follows [26]:

$$P_{PV} = P_{DC} + P_{VSI} \tag{1}$$

where P_{PV} denotes the generated power from the PV modules, P_{VSI} is the injected power from the PV inverter into the grid and P_{DC} is the power flowing through the PV DC-link capacitor (C_1). During the normal operation, the injected AC power from the VSI is equal to the generated DC power by the PV modules if the power loss is neglected, therefore (1) can be redefined as:

$$P_{PV} = P_{VSI} = 3U_g I_g \tag{2}$$

where U_g and I_g are the rated value of the grid voltage and current per phase, respectively. The power balance between the P_{PV} and the P_{VSI} maintains the voltage of the PV DC-link capacitor stable. However, when a grid fault happens, the VSI becomes unable to inject completely the generated power from the PV plant into the grid due to the sudden voltage dip at the PCC. Hence, the excess power causes a severe rise in the DC-link voltage. Mathematically, this fault condition can be represented by [27]:

$$(P_{PV} - P_{VSI\_f})\Delta t = P_{DC}\Delta t = \frac{1}{2}C_1(V_{DC\_f}^2 - V_{DC}^2) \tag{3}$$

$$P_{VSI\_f} = 3V_f I_g \tag{4}$$

TABLE 1. Design parameters of the studied PV/wind hybrid power system.

PV plant		Wind farm	
Parameter	**Value**	**Parameter**	**Value**
Rating power	2 MW	Rating power	4 MW
No. of parallel-connected strings	1320	Turbine type	Gamesa G80
No. of series-connected modules/string	5	Rating power of wind turbine	2 MW
Module type	SunPower SPR-WHT-D	Cut-in speed	3.5 m/s
Peak power/module (P_{max})	305 W	Cut-out wind speed	25 m/s
Solar cells	96 (monocrystalline)	Rated speed	15 m/s
Rated voltage of PV module (V_{mpp})	54.7 V	Rotor diameter	80 m
Rated current of PV module (I_{mpp})	5.58 A	Swept area	5027 m^2
Open-circuit voltage (V_{oc})	64.2 V	No. of blades	3
Short-circuit current of PV moule (I_{sc})	5.96 A`	Max rotor speed	1900 rev/min
Module efficiency	18.7 %	Gearbox stages	3
Dimensions	32*155*128 (mm)	Gearbox ratio	1:101
Weight	18.6 kg	Generator type	DFIG
Electrical utility		Output voltage	0.69 kV
Rated voltage	220 kV	Frequency	50 Hz
Rated frequency	50 Hz	Hub height	78 m
S.C level	1000 MVA	Tower shape	Conical
X/R	8	Tower-type	Steel tube

$$V_{DC\_f} = \sqrt{\frac{2(P_{PV} - 3V_f I_g)\Delta t}{C_1} + V_{DC}^2} \quad (5)$$

where P_{VSI-f} and V_f are the power inserted by the PV inverter and the PCC voltage during the fault, respectively, and Δt denotes the fault duration. V_{DC} and V_{DC-f} are the PV DC-link voltage before and during the fault, respectively. It is evident from (5) that the increasing rate of the DC-link voltage during the grid faults depends on the voltage sag magnitude and the duration of the fault. Therefore, the SRFCL protection scheme is utilized to augment the PCC voltage during the faults so that the overvoltage violation of the PV DC-link can be eliminated.

On the other hand, the generated power and voltage from the DFIG decrease sharply during the transient faults because of the severe voltage drop at the PCC. Thus, according to the swing equation (6) [28], the power imbalance between the input mechanical power and the generated electrical power causes a great disturbance to the rotor speed and electromagnetic torque of the DFIG. The SRFCL protection system is employed to enhance the injected power from the wind farm during the network faults for achieving the desired power balance and improving the transient stability of the DFIG.

$$P_{mech} - P_e = \frac{2H_g}{\omega_s}\frac{d^2\delta}{dt^2} \quad (6)$$

where P_{mech} is the input mechanical power to the wind turbine and P_e is the generated electrical power from the DFIG. H_g, ω_s, and δ are the inertia constant, synchronous speed, and the rotor angle of the DFIG, respectively.

IV. FRT CONTROL SCHEME OF THE HYBRID POWER SYSTEM

In this section, the FRT control scheme implemented to enhance the transient stability and the FRT capability of the hybrid power system during the grid faults is discussed in detail. The FRT scheme of the PV system includes the DC-link voltage suppression by controlling the DC/DC boost converter and also injecting reactive power from the employed inverter to support the PCC voltage. Moreover, the FRT control scheme of the DFIG requires generating reactive power during the grid faults based on the voltage sag level to enhance the system performance and the grid voltage.

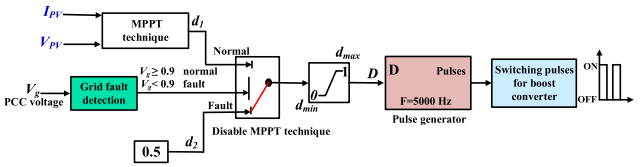

FIGURE 2. Control scheme of the PV DC/DC boost converter.

A. BOOST CONVERTER CONTROL SCHEME

Fig.2 illustrates the control system of the PV DC/DC boost converter. Under normal operation conditions, the Maximum Power Point Tracking (MPPT) technique provides the duty cycle for the boost converter to capture the maximum PV plant power during changing of the irradiance. The implemented MPPT is the modified Incremental Conductance (InCond) algorithm that has been discussed in detail in [29]. But, when a grid fault occurs, the incoming maximum power from the PV modules cannot be inserted entirely into the electrical utility because of the voltage sag at the PCC, so the DC-link voltage boosts sharply.

To eliminate the severe increase in the DC-link voltage during the network faults, the MPPT is deactivated when the fault is detected and the boost converter continues operation with a constant duty cycle, which will eventually reduce

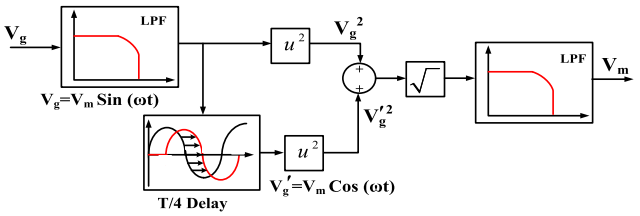

FIGURE 3. Fault detection strategy using the peak value method.

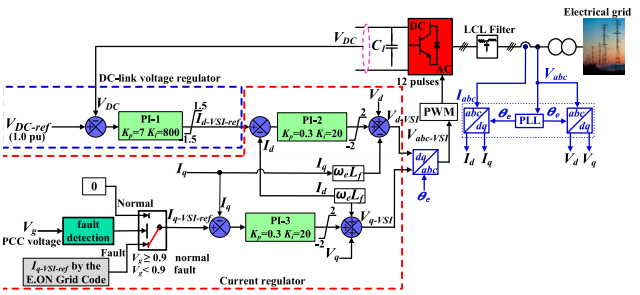

FIGURE 4. Control scheme of the VSI.

the generated power from the PV plant. The fault detection strategy employs the peak value method shown in Fig. 3 [30], which uses the quarter-period (T/4) delay structure to determine the magnitude of voltage drop at the PCC. Therefore, with the non-MPPT mode, the mismatched power between the generated DC power and the injected AC power is minimized so that the PV DC-link voltage can be prevented from reaching very high [12].

B. VSI CONTROL SCHEME

In this paper, a three-phase, three-level Pulse Width Modulation (PWM) Voltage Source Inverter (VSI) is employed to integrate the PV plant with the PCC. Fig. 4 shows the control system for the VSI along with the FRT scheme. This control strategy uses an external voltage regulator that generates the $I_{d-VSI-ref}$ reference current to maintain the PV DC-link voltage constant, while the $I_{q-VSI-ref}$ reference current is employed for controlling the injected reactive power. Under normal operating conditions, the reference reactive current ($I_{q-VSI-ref}$) is set as zero to keep the PV system operation at the unity power factor. However, when there is a grid fault, the injected reactive current is determined according to the E.ON Netz grid code depicted in Fig. 5, for assisting the grid voltage recovery. The injected reactive current during the grid faults can be defined mathematically by [31], [32]:

$$\frac{I_q}{I_n} = \begin{cases} 0, & 0.9\ p.u \le V_g \le 1.1\ p.u \\ k - kV_g, & 0.5\ p.u \le V_g \le 0.9\ p.u \\ 1 & V_g \le 0.5\ p.u \end{cases} \tag{7}$$

$$k = \frac{I_q/I_n}{1 - V_g} \ge 2\ p.u \tag{8}$$

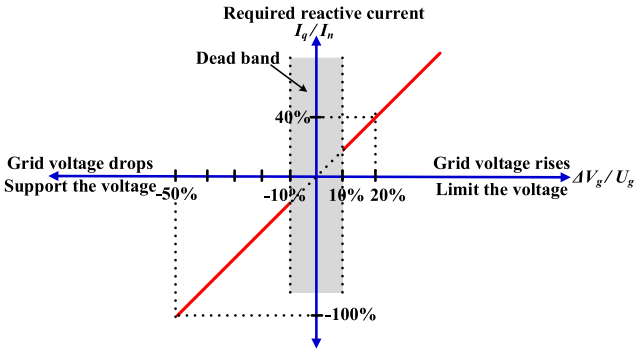

FIGURE 5. Required reactive current to support the voltage during faults [33].

where I_q is the injected reactive current by the PV system during the faults, I_n is the rated current of the VSI and V_g is the PCC voltage.

The internal current regulator compares the $I_{d-VSI-ref}$ and $I_{q-VSI-ref}$ with the injected active and reactive currents (I_d and I_q) for generating the V_{d-VSI} and V_{q-VSI} desired voltage that are then converted into a three-phase modulating voltage to VSI controller. Finally, the control system of the VSI can be described as follows:

$$I_{d\_VSI\_ref} = K_{p\_1}\left(V_{DC\_ref} - V_{DC}\right) + K_{i\_1}\int\left(V_{DC\_ref} - V_{DC}\right)dt \tag{9}$$

$$I_{q\_VSI\_ref} = \begin{cases} 0, & 0.9\ p.u \le V_g \le 1.1\ p.u \\ 2.\mu.I_n, & 0.5\ p.u \le V_g \le 0.9\ p.u \\ I_n & V_g \le 0.5\ p.u \end{cases} \tag{10}$$

$$V_{d\_VSI} = V_d + K_{p\_2}\left(I_{d\_VSI\_ref} - I_d\right) + K_{i\_2}\int\left(I_{d\_VSI\_ref} - I_d\right)dt - \omega_e L_f I_q \tag{11}$$

$$V_{q\_VSI} = V_q + K_{p\_3}\left(I_{q\_VSI\_ref} - I_q\right) + K_{i\_3}\int\left(I_{q\_VSI\_ref} - I_q\right)dt + \omega_e L_f I_d \tag{12}$$

where V_{DC} is the amplitude of the PV DC-link voltage. k_p, k_i are the proportional and integral gains of the PI controller in the VSI control scheme, respectively. μ indicates the depth of voltage dip during the grid faults, L_f is the inductance of the PV system filter, and ω_e represents the rotational speed of the d-q synchronous reference frame. V_d, V_q and I_d, I_q denote d-q axis components of the grid voltage and the injected current from the PV inverter, respectively.

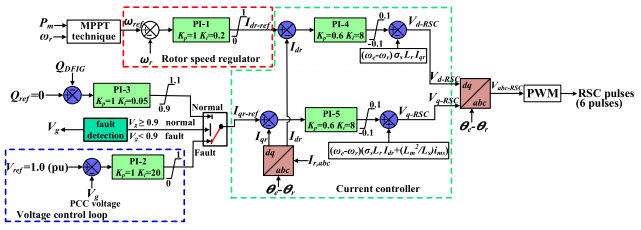

FIGURE 6. Control scheme of the RSC.

C. RSC CONTROL SCHEME

The Rotor side Converter (RSC) of the DFIG is utilized to interface the rotor side with the DC-link capacitor via an IGBT-based two-level six-pulse full-bridge power converter. The main objective of the RSC is to control the injected active and reactive power at the PCC. Fig. 6 shows the control strategy of the RSC. In this work, the speed regulator of the DFIG rotor compares the reference rotational speed produced from the MPPT with the measured rotor speed to provide the reference active current (I_{dr-ref}). This reference current is employed for extracting the maximum generated power by the wind farm during the wind speed variations. The executed MPPT technique in this work is the adaptive Perturb and Observe (P&O) method that has been explained in detail in [29].

Furthermore, the reference reactive current (I_{qr-ref}) is used to control the generated reactive power in such a way that it regulates the PCC voltage to 1.0 per unit (pu). During normal operation conditions, the reference reactive power (Q_{ref}) is imposed as zero for maintaining the DFIG at the unity power factor. On the other hand, when a voltage drop appears due to the grid faults, the I_{qr-ref} is determined based on the voltage sag level so that the reactive power is inserted for supporting the grid voltage. Then, the inner current controller compares the I_{dr-ref} and the I_{qr-ref} with the measured rotor currents (I_{dr} and I_{qr}) for creating the V_{d-RSC} and V_{q-RSC} reference voltage to RSC control [34], [35]. The inner current control loop is designed for improving the dynamic response of the control system to any disturbance. Finally, the RSC control scheme can be described as follows:

$$I_{dr\_ref} = K_{pr\_1}(\omega_{ref} - \omega_r) + K_{ir\_1}\int (\omega_{ref} - \omega_r)dt \tag{13}$$

$$I_{qr\_ref} = K_{pr\_2}\left(V_{ref} - V_g\right) + K_{ir\_2}\int \left(V_{ref} - V_g\right)dt \tag{14}$$

$$V_{d\_RSC} = -(\omega_e - \omega_r)\sigma_s L_r I_{qr} + K_{pr\_4}\left(I_{dr\_ref} - I_{dr}\right) + K_{ir\_4}\int \left(I_{dr\_ref} - I_{dr}\right)dt \tag{15}$$

$$V_{q\_RSC} = (\omega_e - \omega_r)(\sigma_s L_r I_{dr} + \frac{L_m^2}{L_s} i_{ms}) + K_{pr\_5}\left(I_{qr\_ref} - I_{qr}\right) + K_{ir\_5}\int \left(I_{qr\_ref} - I_{qr}\right)dt \tag{16}$$

where ω_{ref}, ω_r denote the reference rotation speed generated from the MPPT and the actual rotation speed of the DFIG rotor, respectively. V_g, V_{ref} is the actual PCC voltage and its reference value (1.0 pu), respectively. L_s, L_r subscribe the self-inductance of the stator and rotor windings, respectively and L_m represents the magnetizing inductance of the DFIG. i_{ms}, σ_s are the stator magnetizing current and the stator leakage factor, respectively.

D. GSC CONTROL SCHEME

The Grid side Converter (GSC) of the DFIG is employed to connect the DC-link side with the electrical grid through an IGBT-based two-level six-pulse full-bridge power converter.

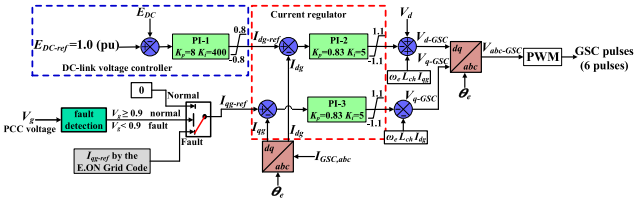

FIGURE 7. Control scheme of the GSC.

The major task of the GSC is to regulate the DC-link voltage of the DFIG at the reference value (1.0 pu) and also control the injected reactive current into the grid. Fig. 7 demonstrates the control scheme of the GSC. In this work, the DC-link voltage controller generates the I_{dg-ref} reference current to obtain a constant DC-link voltage, whereas the I_{qg-ref} reference current is utilized to control the exchanged reactive current with the grid. Under normal operating conditions, the reference reactive current (I_{qg-ref}) is set to zero for keeping the unity power factor at the GSC output; however, it is determined by the E.ON Netz grid code during the faults to enhance the grid voltage. Then, the current regulator compares the I_{dg-ref} and the I_{qg-ref} with the generated GSC currents (I_{dg} and I_{qg}) to estimate the V_{d-GSC} and V_{q-GSC} required voltage to GSC controller [36], [37]. Finally, the control strategy of the GSC can be expressed as:

$$I_{dg\_ref} = K_{pg\_1}\left(E_{DC\_ref} - E_{DC}\right) + K_{ig\_1}\int \left(E_{DC\_ref} - E_{DC}\right)dt \tag{17}$$

$$V_{d\_GSC} = V_d - K_{pg\_2}\left(I_{dg\_ref} - I_{dg}\right) + \omega_e L_{ch} I_{qg} - K_{ig\_2}\int \left(I_{dg\_ref} - I_{dg}\right)dt \tag{18}$$

$$V_{d\_GSC} = -\omega_e L_{ch} I_{dg} - K_{pg\_3}\left(I_{qg\_ref} - I_{qg}\right) - K_{ig\_3}\int \left(I_{qg\_ref} - I_{qg}\right)dt \tag{19}$$

where k_{pg}, k_{ig} represent the proportional and integral gains of the PI controller in the GSC control scheme, respectively. E_{DC}, E_{DC-ref} is the magnitude of the DC-link voltage of the DFIG and its reference value (1 pu), respectively. L_{ch} denotes the inductance of the DFIG filter.

V. SHUNT RESONANCE FAULT CURRENT LIMITER (SRFCL) PROTECTION STRATEGY

In this section, the architecture and the operating principle of the proposed SRFCL protection strategy are discussed. Also, the implemented control system and the methodology for designing the SRFCL parameters are explained in detail.

A. CONFIGURATION OF THE SRFCL

Fig. 8 illustrates the configuration of the SRFCL protection strategy. It includes two distinct parts, namely, the bridge branch and the resonance part, which are described as follows:

1) The bridge branch: This branch is formed by a diode bridge rectifier, D_1-D_4 includes a small DC limiting reactor,

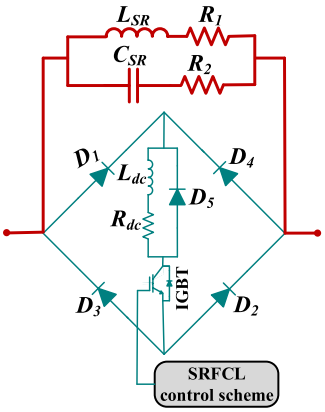

FIGURE 8. Configuration of the SRFCL protection strategy.

L_{dc} connected in series with an IGBT switch. The inherent resistance of the DC reactor is represented by a small series resistor, R_{dc}, and also the free-wheeling diode, D_5 is placed inside the diode bridge to ensure the safe operation for the L_{dc}.

2) The shunt resonance part: This part consists of a parallel combination of an inductor, L_{SR} and a capacitor, C_{SR} connected in series with the resistors R_1 and R_2, respectively. The frequency of the resonance is considered equal to the power system frequency. The design parameters of the SRFCL that achieve the best performance for our work have been determined using the Particle Swarm Optimization (PSO) technique.

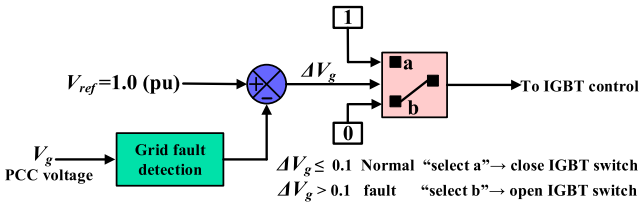

FIGURE 9. Control scheme of the SRFCL.

B. OPERATION PRINCIPLE OF THE SRFCL

In this work, as a protection strategy, the SRFCL is placed in each phase of the three-phase transmission lines near the PCC. The control scheme of the SRFCL is shown in Fig. 9. The voltage dip at the PCC is exploited for fault detection and SRFCL control scheme. During normal operation conditions, the IGBT switch remains closed which allows the total line current to flow through the diode bridge circuit (D_1-D_4). The positive half cycle of the line current takes the path connecting D_1, L_{dc}, R_{dc}, D_2, whereas the negative half cycle passes through D_4, L_{dc}, R_{dc}, and D_3. Therefore, the SRFCL has an insignificant effect during the normal operating since the diodes forward voltage drop is negligible compared to the voltage drop across the transmission lines.

However, when a PCC voltage dip occurs, the IGBT is turned off and the bridge branch becomes an open-circuit, thus the fault current is minimized by passing through the resonance part impedance as illustrated in Eq. (20)-(21). At the same time, the free-wheeling diode (D_5) offers a discharge path for the L_{dc} when the IGBT is opened. The SRFCL permits the evacuation of the generated power from the hybrid system; it also provides a voltage drop that leads to raising the PCC voltage and keeping the hybrid system dynamically stable. Hence, by employing the SRFCL protection strategy, the negative impacts of the grid faults can be eliminated so that the transient stability and the FRT capability of the hybrid power system are enhanced. Then, when the PCC voltage regains its rated value, the IGBT is closed and the system returns to the normal operation.

$$I_f = \frac{|V_g|}{|Z_{SR}|} \tag{20}$$

$$Z_{SR} = \frac{R_1R_2 + (L_{SR}/C_{SR})}{R_1 + R_2} + j\frac{\omega L_{SR} + (R_2 - R_1)}{R_1 + R_2} \tag{21}$$

where I_f is the fault current, V_g is the PCC voltage and Z_{SR} denotes the equivalent impedance of the SRFCL. R_1, R_2, L_{SR}, and C_{SR} represent the resistors, the inductor, and the capacitor of the SRFCL resonance part, respectively.

TABLE 2. Optimal parameters of the SRFCL obtained by the PSO technique.

L_{SR}	R_1	C_{SR}	R_2	L_{dc}	R_{dc}
0.0253 H	0.9759 Ω	498 μF	0.9738 Ω	1 mH	0.3 mΩ

C. DESIGNING OF THE SRFCL PARAMETERS USING PSO

In this study, the optimal parameters of the SRFCL shown in Table 2 have been obtained by using the PSO technique. This optimization algorithm is a population-based stochastic search inspired by the simulation of the social behavior of birds. In the PSO technique, the major agent is referred to as a particle and a group of particles is called swarm or population. Each particle in the swarm is represented by a vector of the position (X) and the velocity (V) that can be considered as a candidate solution for the optimization problem. The position and velocity of each particle are updated based on its best solution and the global best solution associated with other particles according to the following expression [38], [13]:

$$V_i^{j+1} = wV_i^j + c_1r_1(Pbest_i^j - X_i^j) + c_2r_2(Gbest^j - X_i^j) \tag{22}$$

$$X_i^{j+1} = V_i^{j+1} + X_i^j \tag{23}$$

where V, X denote the velocity and the position of the particles in the search space, respectively. i represents the particle number, j is the iteration number, and w is the weight factor employed to control the effect of the previous velocities on the current velocity. r_1, r_2 are uniformly distributed random numbers between [0, 1], C_1 is the cognition learning factor, and C_2 is the social learning factor. Also, $Pbest_i^j$ represents the particle's best position and $Gbest^j$ represents the global best position found by all particles of the swarm.

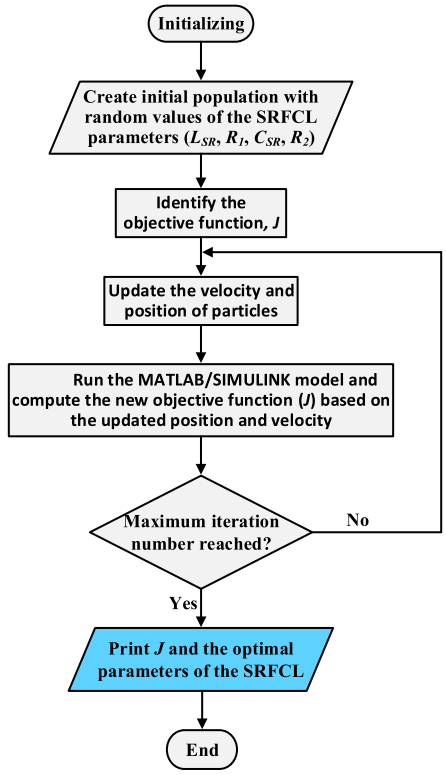

FIGURE 10. Flowchart for designing the optimal SRFCL parameters using PSO.

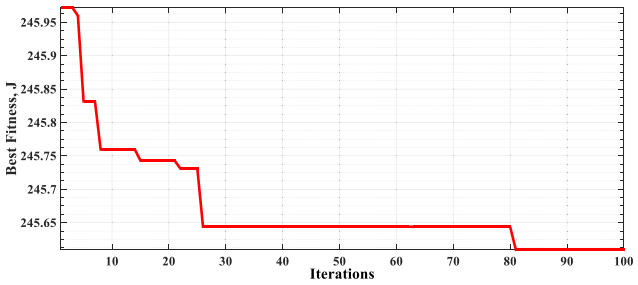

FIGURE 11. Convergence of the objective function using PSO.

Fig. 10 illustrates the PSO flowchart for designing the optimal parameters of the SRFCL while minimizing the objective function (J) during any fault condition. Moreover, the convergence curve of the objective function is shown in Fig. 11. The SRFCL parameters are optimized by achieving the following objective functions:

$$O_{bj1} = Min\,(\Delta V_g) \tag{24}$$
$$O_{bj2} = Max\,(P_{hybrid})\ or \tag{25}$$
$$O_{bj2} = Min\,(P^*_{hybrid}), \quad \text{where } P^*_{hy} = (1/P_{hybrid}) \tag{26}$$
$$O_{bj3} = Min\,(Q_{hybrid}) \tag{27}$$
$$O_{bj4} = Min\,(\Delta V_{DC}) \tag{28}$$
$$O_{bj5} = Min\,(\Delta E_{DC}) \tag{29}$$
$$J = Min(O_{bj1}, O_{bj2}, O_{bj3}, O_{bj4}, O_{bj5}) \tag{30}$$

where *Min* represents the minimization objective function and *Max* represents the maximization objective function. ΔV_g, ΔV_{DC}, ΔE_{DC} denote the disturbance of the PCC voltage, the DC-link voltage of the PV, and the DFIG DC-link voltage, respectively. P_{hybrid}, Q_{hybrid} are the injected active power and reactive power from the hybrid system, respectively.

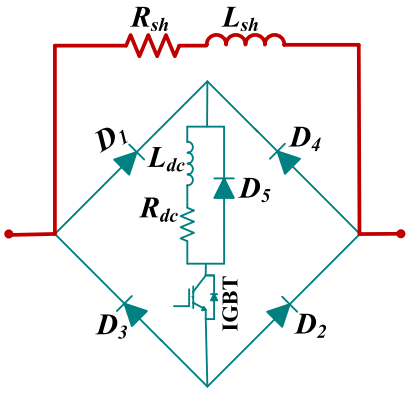

FIGURE 12. Configuration of the BFCL.

VI. BRIDGE FAULT CURRENT LIMITER (BFCL)

Since the performance of the proposed SRFCL protection strategy will be analyzed compared with that of the conventional BFCL, it is necessary to discuss its construction and the working principle. The main drawback of the conventional BFCL compared to the proposed SRFCL is that it provides less effective impedance for the power evacuation during severe grid faults since it comprises only current limiting inductance along with one series resistor [21], as shown in Fig. 12. The values of the R_{sh} and the L_{sh} are selected to be 0.976 Ω and 0.028 H, respectively that achieve the best system performance and satisfy Eq. (31)-(32) [39]. Also, the control system of the BFCL is the same as that of the SRFCL, as illustrated in Fig. 9. At normal operating conditions, the IGBT switch remains closed and the bridge branch carries the line current. However, when a grid fault occurs, the IGBT switch is turned off by the control circuit so that the shunt impedance enters the faulted line to limit the fault current. Although the control scheme for both the SRFCL and the BFCL is the same, the impedance imposed by the proposed SRFCL has more impact than the conventional BFCL, because of the presence of the capacitor and the additional resistor.

$$R_{sh} \geq \frac{V_{pcc}^2 + \sqrt{V_{pcc}^4 - P_g^2 X_{sh}^2}}{P_g} \tag{31}$$
$$X_{sh} < \frac{V_{pcc}^2}{P_g} \tag{32}$$

VII. SIMULATION RESULTS AND DISCUSSIONS

In this work, the dynamic performance of the hybrid power system is evaluated during both symmetrical and

unsymmetrical grid faults to validate the effectiveness of the proposed SRFCL strategy in the enhancement of the FRT capability and transient stability. The symmetrical faults [three-line-to-ground (3LG) and three-phase voltage sag] and the unsymmetrical faults [double-line-to-ground (2LG) and line-to-ground (1LG)] occur at beginning of the transmission line (F1 location) as depicted in Fig. 1. This fault location has the greatest impact on the hybrid power system since being the nearest point to the PCC. The simulation study is executed using the MATLAB/SIMULINK software and the simulation scenarios are conducted for separate six cases, namely,

1) Case 1: without any protection scheme
2) Case 2: with FRT control scheme
3) Case 3: with BFCL
4) Case 4: With the FCL topology suggested in [18] consisting of a parallel combination of capacitor and inductor, $C = 300\ \mu$F, $L = 38$ mH
5) Case 5: With the FCL topology presented in [19] consisting of a parallel combination of capacitor and inductor, $C = 50\ \mu$F, $L = 141$ mH
6) Case 6: with optimal SRFCL

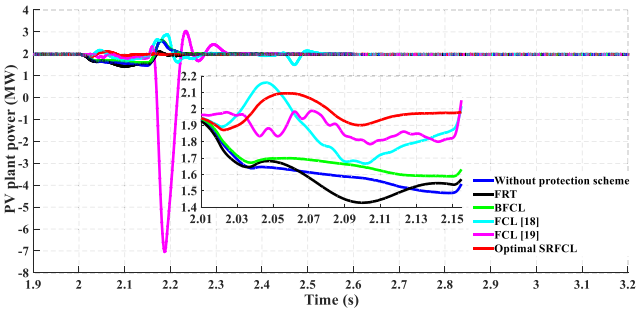

(a) Generated active power by the PV plant (P_{pv}).

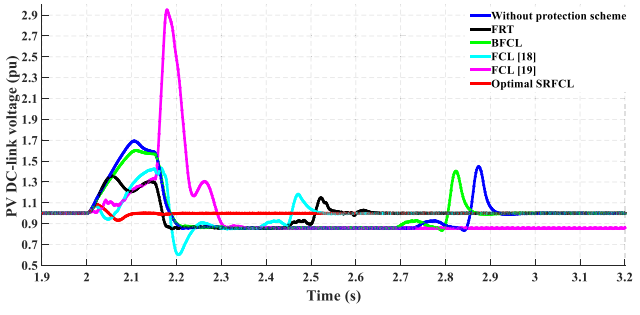

(b) PV DC-link voltage (V_{DC}).

FIGURE 13. **Effect of the voltage sag on the PV plant stability.**

A. EFFECT OF THE THREE-PHASE VOLTAGE SAG

In the following, the dynamic behavior of the hybrid power system is analyzed during the occurrence of a three-phase voltage sag. The sag depth is 50% of the grid voltage (i.e. PCC voltage drops to 0.5 pu) occurring at t = 2 s and lasting for 150 ms [40]. Fig. 13 (a) depicts the generated active power by the PV plant. It can be seen that without the series protection schemes (i.e. without any protection scheme or with FRT), the generated power declines considerably to 1.57 MW during the voltage sag. Also, with the FCL topologies presented in [18], [19], the generated power drops to 1.67 MW and 1.81 MW, respectively. Besides, when the FCL topology in [18] is employed, the generated power fluctuates sharply after sag clearance. However, with the proposed SRFCL, the injected power by the PV plant improves significantly to 1.9 MW as compared to 1.64 MW with the conventional BFCL. This means the injected active power from the PV plant is increased by 17.37% when the optimal SRFCL strategy is utilized. Fig. 13 (b) illustrates the impact of voltage dip on the DC-link voltage of the PV system. Without any protection scheme in the system, the PV DC-link voltage overshoots sharply to 1.7 pu as compared to 1.6 pu with the BFCL and 1.2 pu with the FRT scheme. Also, with the FCL topologies suggested in [18], [19], the PV DC-link voltage increases severely to 1.43 pu and 2.95 pu, respectively. Moreover, after the voltage sag is cleared, without the SRFCL strategy, the DC-link voltage takes a long time to retrieve its nominal value, where it reaches the steady-state value at t = 2.9 s without protection, t = 2.86 s with BFCL, t = 2.6 s with FRT, and t = 2.5 s with FCL in [18]. In contrast, when the optimal SRFCL is employed, the overshoot of the DC-link voltage is eliminated so that it reaches its rated value once the grid voltage sag is cleared.

Fig. 14 (a) shows the real power injected into the grid by the wind farm. Without the SRFCL protection system, the inserted power drops down significantly to about 2.12 MW during the sag occurrence. Also, it is clear that with the FCL topologies presented in [18], [19], the generated power from the wind farm fluctuates sharply during and after sag occurrence. However, when the optimal SRFCL strategy is employed, the injected power improves considerably to 2.61 MW and rapidly returns to the rating value of 4 MW after sag clearance.

Fig. 14 (b) demonstrates that when the SRFCL is utilized, the absorbed reactive power from the wind farm after fault clearance is reduced substantially by 2.38 MVAR (2.28 MVAR with the SRFCL compared with 4.66 MVAR without any protection scheme). Besides, when the FCL topologies suggested in [18], [19] are employed, the absorbed reactive power after sag clearance increases greatly to 5.97 MVAR and 8.65 MVAR, respectively. Also, it is clear from Fig. 14 (c) that with the SRFCL protection scheme, the oscillations of the DFIG DC-link voltage (E_{DC}) are minimized noticeably during and after voltage drop occurrence. Fig. 14 (d) shows the response of the wind turbine mechanical torque to the voltage sag. In the three cases: without protection scheme, with FRT, and with the BFCL, the output mechanical torque decreases to 0.61 pu, also it drops dramatically to 0.48 pu with the FCL topology introduced in [19]. However, the mechanical torque improves to 0.72 pu and 0.84 pu when the optimal SRFCL and the FCL topology in [18] are utilized, respectively. Fig. 14 (e) demonstrates that without the SRFCL, the DFIG rotor speed overshoots sharply to 1.53 pu since the injected power reduces severely during the sag and the input mechanical power cannot be

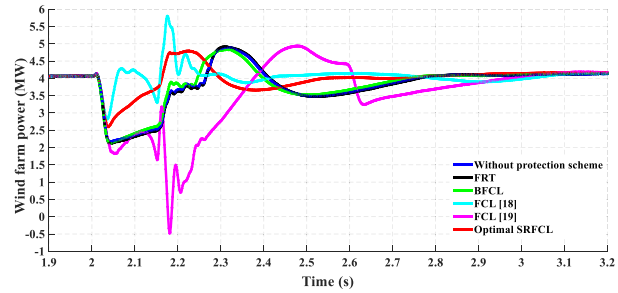

(a) Generated active power by the wind farm (P_{wind}).

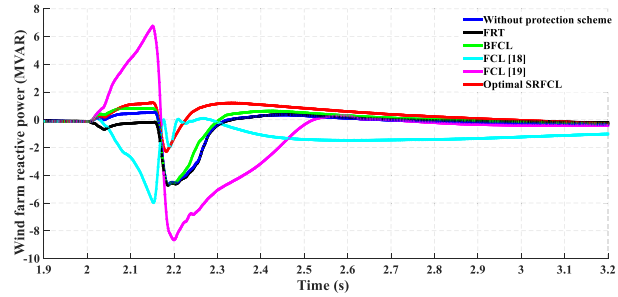

(b) Wind farm reactive power (Q_{wind}).

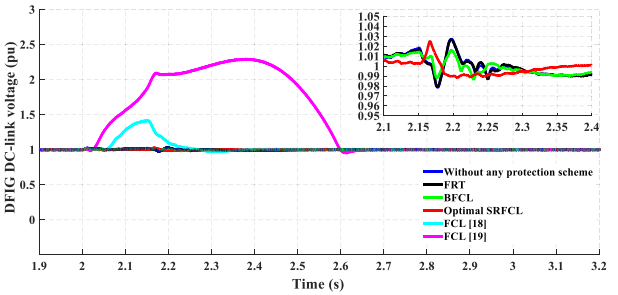

(c) DC-link voltage of the DFIG (E_{DC}).

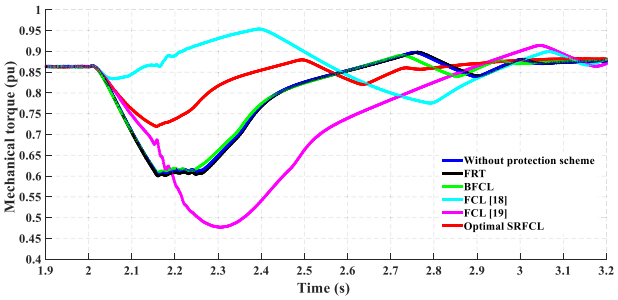

(d) Mechanical torque of the wind turbine (T_m).

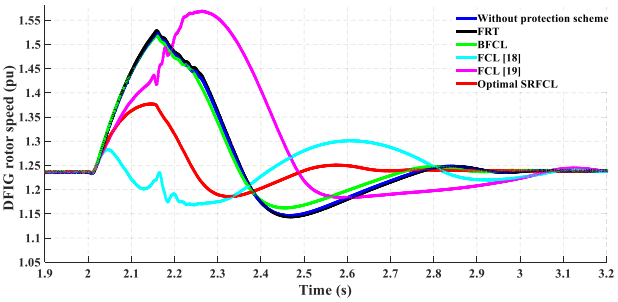

(e) DFIG rotor speed (ω_r).

FIGURE 14. **Effect of the voltage sag on the wind farm stability.**

transformed completely to electrical power, as illustrated in Eq. (6). Although the overshoot of the rotor speed is reduced significantly with the FCL topology employed in [19], it fluctuates greatly after fault clearance. In contrast, when the optimal SRFCL protection strategy is applied, the overshoot is lowered by 0.16 pu so that it rapidly returns to the nominal value (1.2 pu) after fault clearance.

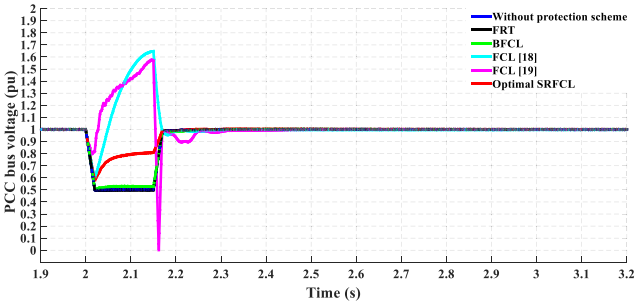

(a) Voltage response at the PCC (V_g).

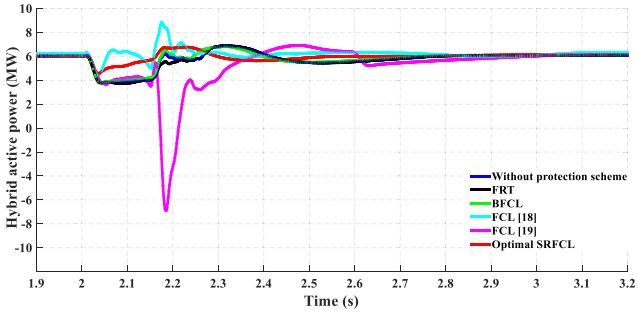

(b) Generated active power by the hybrid system (P_{hybrid}).

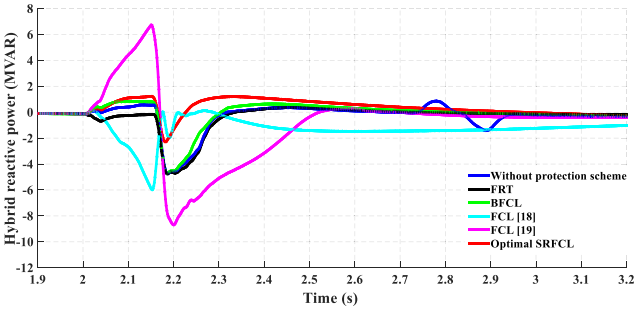

(c) Hybrid system reactive power (Q_{hybrid}).

FIGURE 15. **Transient stability analysis of the hybrid system at the PCC during voltage sag.**

Fig. 15 (a) illustrates the role of the SRFCL in supporting the voltage at the PCC bus. Without the series protection schemes (i.e. without any protection scheme or with the FRT), the PCC voltage declines sharply to 0.5 pu during the voltage sag occurrence.

Also, when the FCL topologies suggested in [18], [19] are employed, the PCC voltage overshoots sharply to about 1.6 pu. However, with the optimal SRFCL, the voltage improves significantly to 0.79 pu as compared to 0.53 pu with the BFCL. Fig. 15 (b) shows the real power inserted

TABLE 3. Transient stability analysis during three-phase voltage sag.

	P_{pv} (MW)	PV DC-link voltage (pu)	P_{wind} (MW)	Q_{wind} (absorbed) (MVAR)	T_m (pu)	ω_r (overshoot) (pu)	PCC voltage V_g (pu)	P_{hybrid} (MW)	Q_{hybrid} (MVAR)
Without protection scheme	1.57	1.7	2.17	4.66	0.613	1.523	0.5	3.74	4.73
FRT	1.43	1.2	2.11	4.72	0.607	1.528	0.5	3.54	4.74
BFCL	1.64	1.6	2.13	4.69	0.618	1.518	0.53	3.77	4.69
FCL [18]	1.67	1.43	Fluctuates	5.97	0.84	1.28	1.65	Fluctuates	5.98
FCL [19]	1.81	2.95	Fluctuates	8.65	0.48	1.57	1.57	Fluctuates	8.68
Optimal SRFCL	1.9	1	2.61	2.28	0.72	1.37	0.79	4.51	2.28

into the grid by the hybrid system during the voltage dip. It is evident that when the SRFCL protection scheme is deactivated, the injected power drops substantially to 3.7 MW, while it improves significantly to 4.51 MW with the SRFCL strategy.

Moreover, with the FCL topologies introduced in [18], [19], the injected power by the hybrid system fluctuates severely during and after voltage sag occurrence. Fig. 15 (c) demonstrates the absorbed reactive power by the hybrid system after the voltage sag clearance. It is evident that when the optimal SRFCL is employed, the absorbed reactive power increases only to 2.28 MVAR while increasing severely to 5.98 MVAR and 8.68 MVAR with the FCL topologies presented in [18], [19], respectively.

From the Figs. 13, 14, and 15, it can be noticed that the transient stability of the hybrid power system has been significantly enhanced during the voltage sag occurrence with the optimal SRFCL protection strategy compared to other cases. Moreover, the transient stability performance of the hybrid power system during the three-phase voltage sag is summarized in Table 3.

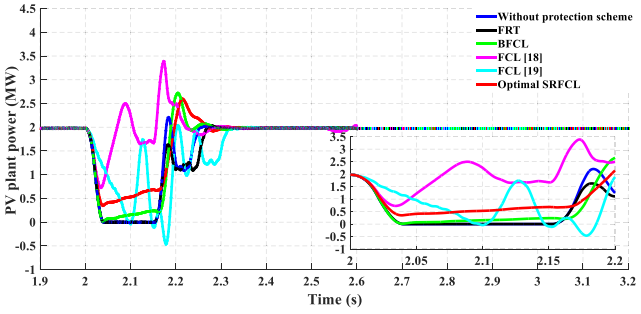

FIGURE 16. Generated active power by the PV plant during 3LG fault.

B. EFFECT OF THE 3LG FAULT

In this subsection, the impact of the proposed SRFCL protection strategy on the transient stability performance of the hybrid power system is validated during the 3LG fault occurrence. The fault occurs at the beginning of the transmission line (F1 location) near the PCC bus at t = 2 s and lasts for 150 ms [41]. Fig. 16 depicts the PV plant power. It is clear that without any series protection scheme (i.e. without any protection scheme or with FRT), the injected power by the PV system reaches a very low value during the fault. Also, with the FCL topologies suggested in [18], [19], the injected power fluctuates severely during the fault occurrence. However, when the optimal SRFCL is utilized, the PV plant power improves considerably to 0.53 MW as compared to 0.16 MW with the BFCL. Furthermore, Fig. 17 (a) shows that when the FCL topologies presented in [18], [19] are employed, the generated active power by the wind farm oscillates greatly during the 3LG fault occurrence. But, with the optimal SRFCL strategy, the wind farm power increases by 0.8 MW as compared to other cases. Fig. 17 (b) demonstrates that when the SRFCL is utilized, the reactive power absorbed by the wind farm after the fault clearance is reduced by 1.55 MVAR (3.1 MVAR with the SRFCL compared with 4.65 MVAR without any protection scheme). Also, it is evident that with the FCL configurations in [18], [19], the absorbed reactive power increases to about 7.5 MVAR.

Fig. 17 (c) illustrates that with the FRT control scheme, the overshoots of the DFIG DC-link voltage are minimized substantially during the 3LG fault so that it quickly returns to the rated value after the fault is cleared. This sharp increase in the voltage happens because of the mismatched power between the GSC and RSC since the fault prevents the RSC from injecting the entire power generated from the wind farm into the grid. Fig. 17 (d) depicts the disturbance of the wind turbine mechanical torque during the 3LG fault. It is evident that without the SRFCL, the generated mechanical torque decreases sharply to 0.32 pu, while it improves to 0.4 pu when the SRFCL strategy is applied. Also, although the output mechanical torque is enhanced significantly with the FCL topology employed in [18], it fluctuates severely after fault clearance. Also, Fig. 17 (e) shows that the overshoot of the DFIG rotor speed is decreased considerably by 0.11 pu and 0.42 pu using the optimal SRFCL and the FCL topology in [18], respectively.

Fig. 18 (a) illustrates the effect of the 3LG fault on the PCC bus voltage. It is clear that without the series protection methods (i.e. without any protection scheme or with FRT), the PCC voltage goes abruptly near zero during the fault occurrence. Also, when the FCL configuration suggested in [18] is utilized, the voltage overshoots sharply to

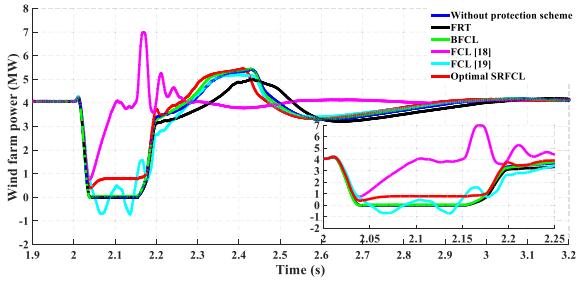

(a) Generated active power by the wind farm (P_{wind}).

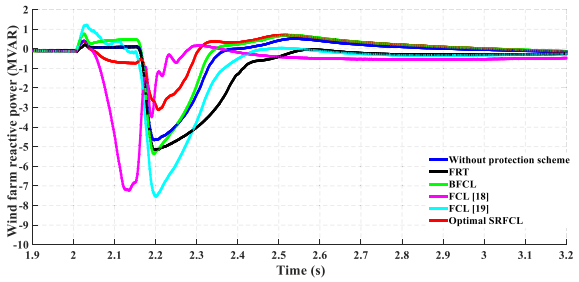

(b) Wind farm reactive power (Q_{wind}).

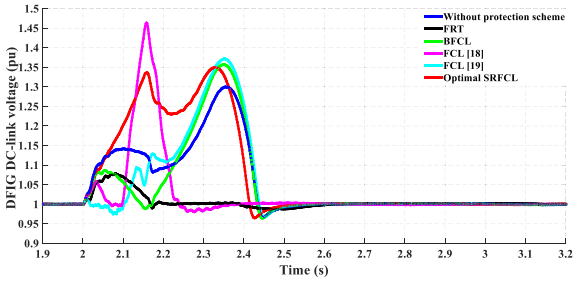

(c) DC-link voltage of the DFIG (E_{DC}).

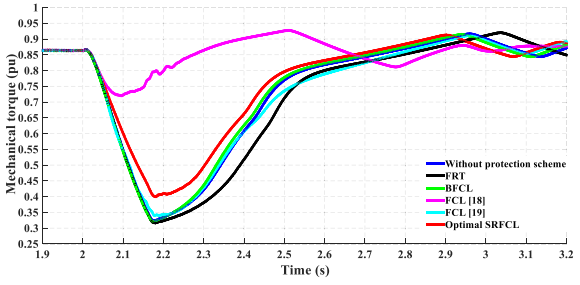

(d) Mechanical torque of the wind turbine (T_m).

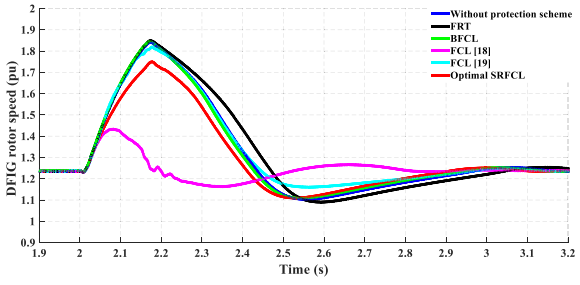

(e) DFIG rotor speed (ω_r).

FIGURE 17. Effect of the 3LG fault on the wind farm stability.

about 1.67 pu while oscillating severely with the FCL topology in [19]. However, with employing the optimal SRFCL,

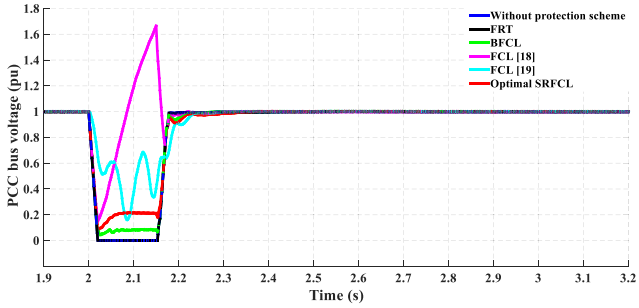

(a) Voltage response at the PCC (V_g).

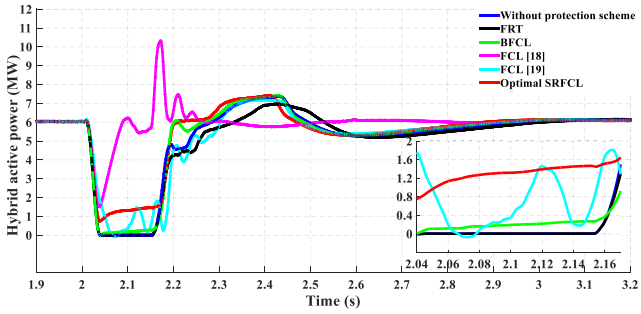

(b) Generated active power by the hybrid system (P_{hybrid}).

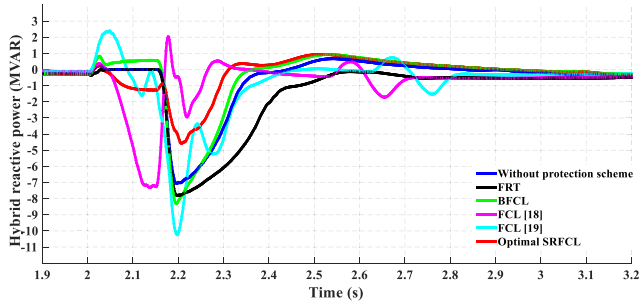

(c) Hybrid system reactive power (Q_{hybrid}).

FIGURE 18. Transient stability analysis of the hybrid system at the PCC during 3LG fault.

the voltage level raises considerably to 0.22 pu as compared to 0.08 pu with the BFCL. Fig. 18 (b) demonstrates the active power injected from the hybrid power system to the electrical network during the fault occurrence. It is obvious that without any protection scheme, the injected active power declines substantially to a very small value, while it improves considerably to 1.3 MW with the optimal SRFCL strategy compared to only 0.2 MW with the BFCL. Moreover, when the FCL topologies presented in [18], [19] are employed, the injected active power fluctuates greatly during the 3LG fault occurrence. Fig. 18 (c) shows that when the optimal SRFCL is utilized, the absorbed reactive power from the hybrid system after fault clearance is decreased by 2.48 MVAR (4.57 MVAR with the SRFCL compared with 7.05 MVAR without any protection scheme). Besides, with the FCL configurations in [18], [19], the absorbed reactive power rises sharply to 7.3 MVAR and 10.2 MVAR, respectively.

It is clear from the comparative transient responses shown in Fig. 16, 17, and 18 that the optimal SRFCL provides a superior transient stability performance system than other cases during the occurrence of the 3LG fault. Moreover, Table 4 summarizes the transient stability performance of the hybrid power system during the 3LG fault.

C. EFFECT OF THE 2LG FAULT

The transient stability performance of the hybrid power system is evaluated during a 2LG fault event to validate the credibility of the proposed SRFCL protection strategy during the unsymmetrical faults. The 2LG fault is considered to happen at the F1 location near the PCC bus within the period from t = 2 s to t = 2.15 s [41].

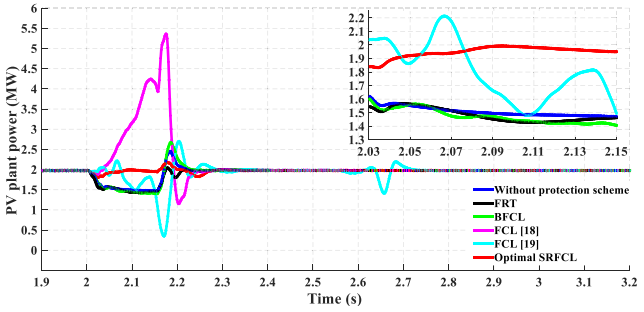

(a) Generated active power by the PV plant (P_{pv}).

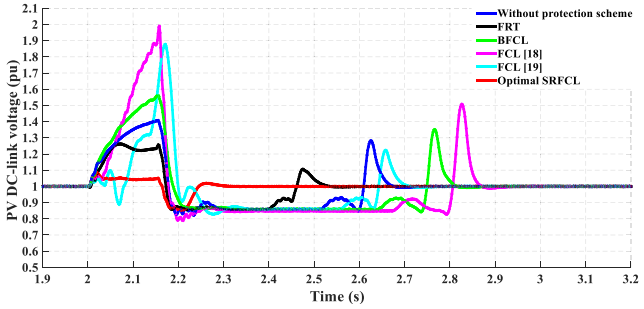

(b) PV DC-link voltage (V_{DC}).

FIGURE 19. Effect of the 2LG fault on the PV plant stability.

Fig. 19 (a) depicts the generated real power by the PV plant during the fault. Without the optimal SRFCL protection strategy, the generated power decreases considerably to 1.48 MW under the fault condition and it overshoots considerably to 2.45 MW and 2.67 MW without any protection scheme and with the BFCL, respectively.

Also, it is evident that when the FCL topology in [18] is employed, the generated power overshoots sharply to 5.36 MW while fluctuating severely with the FCL configuration in [19]. In contrast, when the optimal SRFCL is utilized, the PV plant continues to deliver the rated power (2 MW) during the fault and also the overshoot is minimized substantially after fault clearance. Fig. 19 (b) illustrates that the 2lG fault causes a great disturbance to the PV DC-link voltage. With the FCL topologies suggested in [18], [19], the DC-link voltage overshoots sharply to about 2 pu as compared to 1.56 pu with BFCL, 1.41 pu without any protection

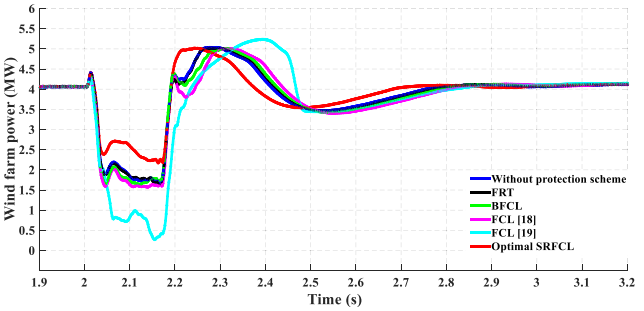

(a) Generated active power by the wind farm (P_{wind}).

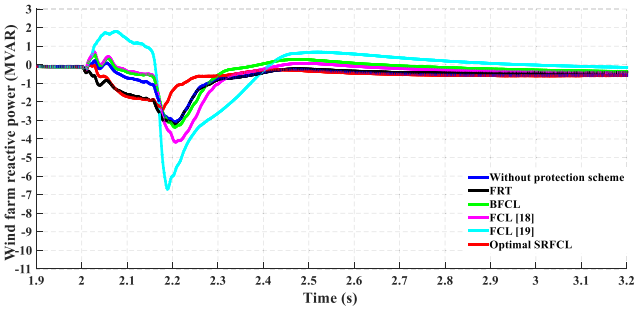

(b) Wind farm reactive power (Q_{wind}).

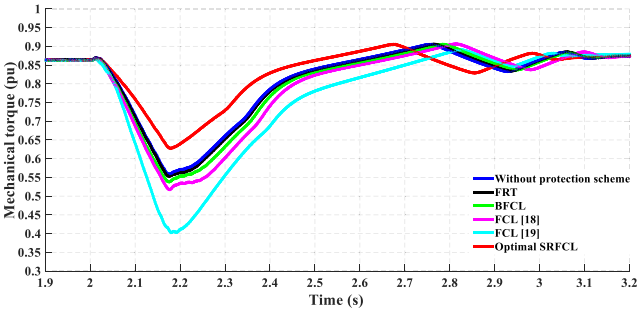

(c) Mechanical torque of the wind turbine (T_m).

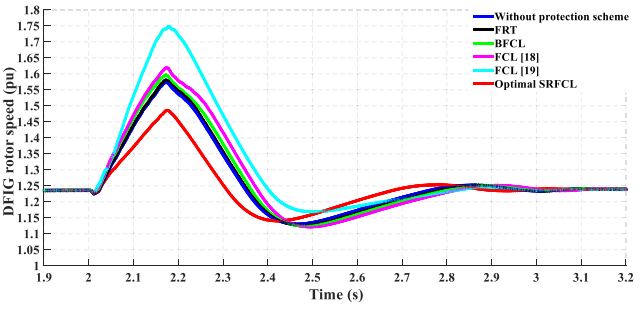

(d) DFIG rotor speed (ω_r).

FIGURE 20. Effect of the 2LG fault on the wind farm stability.

system, and 1.26 pu with the FRT scheme. Also, the voltage takes a long period to restore the nominal value after fault clearance, where it reaches the steady-state value at t = 2.87 s and t = 2.71 s with the FCL configurations in [18], [19], respectively. Besides, the rated value is restored at t = 2.8 with the BFCL, t = 2.67 s without any protection scheme, and t = 2.5 s with the FRT. But, when the optimal SRFCL is

TABLE 4. Transient stability analysis during 3LG fault.

	P_{pv} (MW)	P_{wind} (MW)	Q_{wind} (absorbed) (MVAR)	DFIG DC-link voltage (pu)	T_m (pu)	ω_r (overshoot) (pu)	PCC voltage V_g (pu)	P_{hybrid} (MW)	Q_{hybrid} (MVAR)
Without protection scheme	0	0	4.65	1.3	0.325	1.842	0	0	7.05
FRT	0	0	5.15	1	0.317	1.849	0	0	7.8
BFCL	0.16	0.04	5.36	1.36	0.322	1.845	0.08	0.2	8.3
FCL [18]	Fluctuates	Fluctuates	7.2	1.46	0.34	1.43	1.67	Fluctuates	7.3
FCL [19]	Fluctuates	Fluctuates	7.5	1.37	0.72	1.82	Fluctuates	Fluctuates	10.2
Optimal SRFCL	0.53	0.8	3.1	1.35	0.4	1.74	0.22	1.3	4.57

TABLE 5. Transient stability analysis during 2LG fault.

	P_{pv} (MW)	PV DC-link voltage (pu)	P_{wind} (MW)	Q_{wind} (absorbed) (MVAR)	T_m (pu)	ω_r (overshoot) (pu)	PCC voltage V_g (pu)	P_{hybrid} (MW)	Q_{hybrid} (MVAR)
Without protection scheme	1.49	1.41	1.88	3.09	0.56	1.57	0.49	3.3	3.22
FRT	1.43	1.26	1.88	3.19	0.55	1.58	0.49	3.27	3.04
BFCL	1.44	1.56	1.66	3.36	0.54	1.6	0.48	3.17	3.26
FCL [18]	5.36 (overshoot)	2	1.6	4.17	0.52	1.62	2	11.1 (overshoot)	5.94
FCL [19]	Fluctuates	1.88	0.79	6.7	0.4	1.75	0.15	Fluctuates	10.17
Optimal SRFCL	2	1.04	2.4	2.43	0.63	1.48	0.66	4.59	2.27

employed, the overshoot of the DC-link voltage is diminished significantly so that it quickly returns to the rated value at t = 2.26 s.

Fig. 20 (a) demonstrates the active power generated by the wind farm during the 2LG fault. When the optimal SRFCL is utilized, the active power is enhanced substantially to 2.4 MW as compared to only 0.79 MW with the FCL topology in [19] and 1.6 MW with other protection schemes. Fig. 20 (b) shows that with the SRFCL protection system, the absorbed reactive power from the wind farm after fault clearance is declined significantly by 4.27 MVAR (2.43 MVAR with the SRFCL compared with 6.7 MVAR with the FCL configuration in [19]). Fig. 20 (c) depicts the response of the wind turbine mechanical torque to the 2LG fault. When the FCL topology in [19] is employed, the output mechanical torque declines sharply to 0.4 pu, however, it improves considerably to 0.63 pu with the optimal SRFCL compared to only 0.5 pu with other cases. Moreover, Fig. 20 (d) shows that with the utilization of the SRFCL strategy, the overshoot of the DFIG rotor speed under the fault condition is lowered by 0.27 pu compared with the FCL topology in [19].

Fig. 21 (a) demonstrates the role of the SRFCL in enhancement the voltage at the PCC bus. When the FCL topology in [18] is employed, the voltage overshoots sharply to 2 pu, while it drops severely to 0.15 pu with the FCL in [19]. However, by implementing the proposed SRFCL strategy, the PCC voltage improves significantly to 0.66 pu as compared to only 0.49 pu with other cases. Fig. 21 (b) shows the injected active power from the hybrid system to the PCC bus during the 2LG fault occurrence. It can be mentioned that when the FCL configuration in [18] is used, the injected active power overshoots sharply to 11.1 MW while oscillating greatly with the FCL topology in [19]. On the other hand, the injected power is increased by about 28% with the optimal SRFCL, where it reaches 4.59 MW with the SRFCL compared to only 3.3 MW with other cases. Fig. 21 (c) illustrates that with the SRFCL strategy, the reactive power absorbed from the hybrid system is declined significantly by 7.9 MVAR (2.27 MVAR with the SRFCL compared with 10.17 MVAR with the FCL topology in [19]. Also, when the FCL in [18] is employed, the absorbed reactive power increases greatly to 5.94 MVAR compared to only 3.3 MVAR with other cases.

It is evident from the comparative results shown in Figs. 19, 20, and 21 that the optimal SRFCL strategy is more effective than other protection schemes in improving the transient stability of the hybrid power system during the 2LG fault. Moreover, the transient stability performance of the hybrid power system during the 2LG fault is summarized in Table 5. It is obvious that with the FCL topology in [19], the system performance is the worst among the conducted six cases. Also, compared to the FCL configuration in [18], FRT, and the conventional BFCL, the optimal SRFCL strategy enhances significantly the FRT capability and improves substantially the transient stability of the hybrid power system during the grid faults.

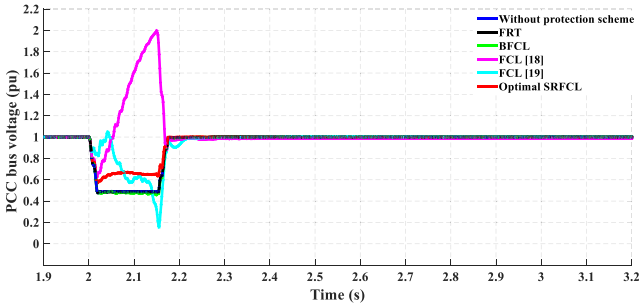

(a) Voltage response at the PCC (V_g).

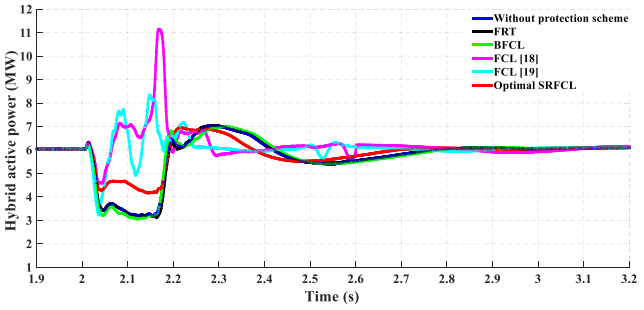

(b) Generated active power by the hybrid system (P_{hybrid}).

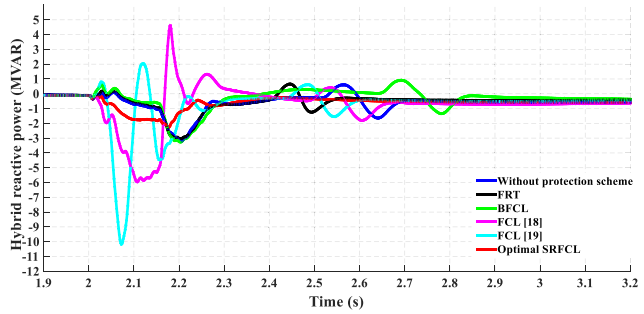

(c) Hybrid system reactive power (Q_{hybrid}).

FIGURE 21. Transient stability analysis at the PCC during 2LG fault.

D. EFFECT OF THE 1LG FAULT

Stability analysis of the hybrid power system with the optimal SRFCL protection scheme is also investigated regarding the 1LG fault since being the most common fault in comparison to the symmetrical faults. Fig. 22 (a-d) shows the responses of mechanical torque, DFIG rotor speed, hybrid active power, and the PCC voltage for the 1LG fault.

From the figures, it can be noticed that the hybrid power system is less affected by the 1LG fault since being the least severe among all grid faults. Moreover, the proposed SRFCL strategy is the most effective in enhancing the transient stability and the FRT capability of the hybrid power system. Table 6 summarizes the transient stability analysis of the system during the 1LG fault.

E. PV PLANT CONNECTION ONCE THE LVRT CONDITION ARRIVED

This subsection investigates the effectiveness of the proposed SRFCL in enhancement the transient stability of the PV plant

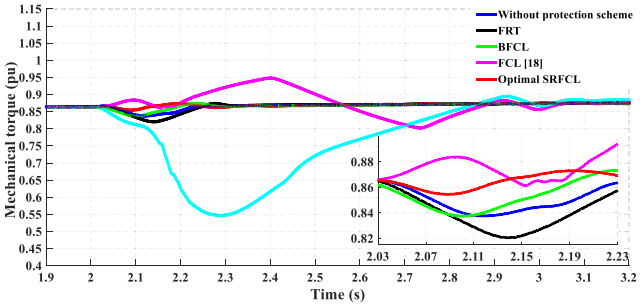

(a) Mechanical torque of the wind turbine (T_m).

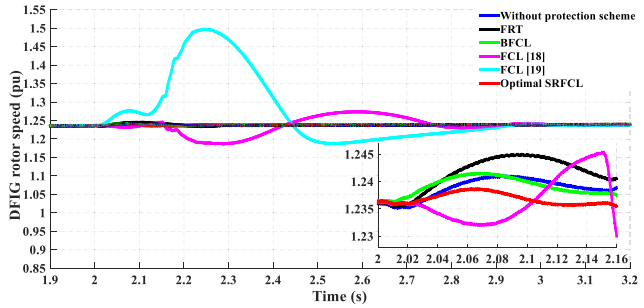

(b) DFIG rotor speed (ω_r).

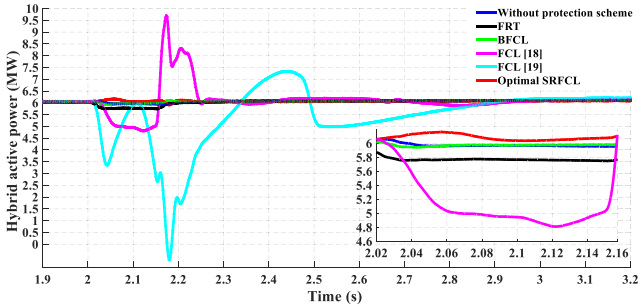

(c) Generated active power by the hybrid system (P_{hybrid}).

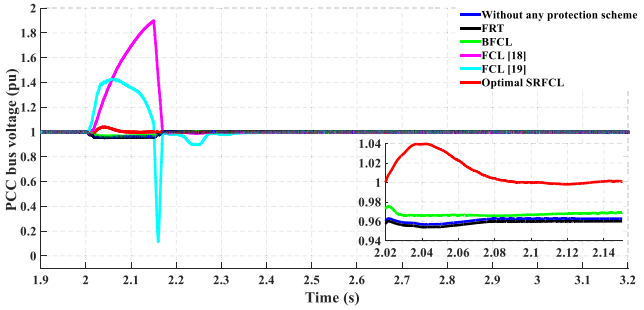

(d) Voltage response at the PCC (V_g).

FIGURE 22. Transient stability analysis of hybrid system during 1LG fault.

when connected once the Low Voltage Ride Through (LVRT) condition arrived. Fig. 23 (a) shows the generated active power from the PV plant. Without the SRFCL strategy, the generated power overshoots sharply during the LVRT, and also it decreases substantially to a very low value (about 0.2 MW) after the LVRT clearance. However, when the proposed SRFCL is employed, the overshoot of the generated power during the LVRT is reduced considerably so that the PV plant injects the rating power (2 MW) after the LVRT clearance. On the other hand, Fig. 23 (b) illustrates that with

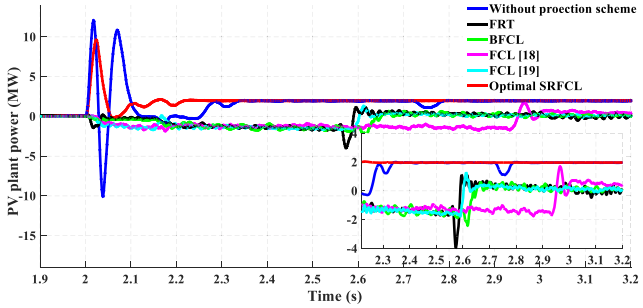

(a) Generated active power by the PV plant (P_{pv}).

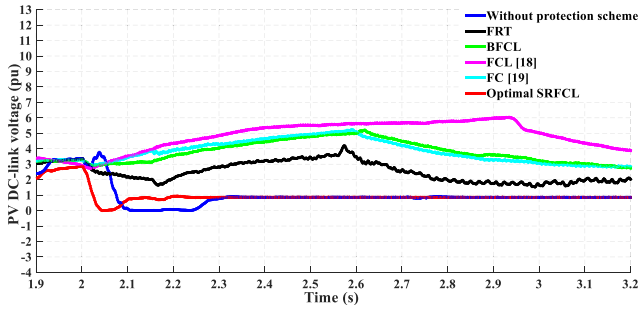

(b) PV DC-link voltage (V_{DC}).

FIGURE 23. PV plant connected once the LVRT condition arrived.

the proposed SRFCL, the disturbance of the DC-link voltage is eliminated significantly so it remains at the rated value (1 pu) once the LVRT is cleared.

TABLE 6. Transient stability analysis during 1LG fault.

	T_m (pu)	ω_r *(pu)*	P_{hybrid} (MW)	PCC voltage V_g (pu)
Without protection	0.838	1.24	5.97	0.957
FRT	0.82	1.245	5.77	0.954
BFCL	0.837	1.242	5.98	0.966
FCL [18]	Fluctuates	Fluctuates	4.95	1.9 (overshoot)
FCL [19]	Fluctuates	Fluctuates	Fluctuates	1.4 (overshoot)
Optimal SRFCL	0.85	1.23	6	1

VIII. CONCLUSION

This paper proposed the employment of an optimal SRFCL protection strategy to augment the transient stability and the FRT capability of a grid-tied hybrid power system during the grid faults occurrence. The design parameters of the SRFCL have been optimized by using the PSO algorithm. The effectiveness of the SRFCL protection strategy is tested during both symmetrical faults such as three-phase voltage sag and 3LG fault and unsymmetrical faults such as 2LG fault and 1LG fault. Also, its performance is compared with that of the FRT control scheme, the conventional BFCL, and different topologies of the FCL suggested in the literature review. Based on the simulation results and discussions, the following points are noteworthy.

(a) The proposed SRFCL strategy ensures the FRT capability augmentation and the transient stability improvement of the hybrid system during all the applied faults.

(b) The generated active power from the hybrid system and the grid voltage are improved significantly with the utilization of the optimal SRFCL.

(c) The SRFCL has a great impact on the DFIG stability by minimizing considerably the overshoot of the rotor speed.

(d) The performance of the optimal SRFCL is superior to that of the BFCL and the FRT control schemes in all characteristics.

In our future work, the proposed SRFCL topology will be validated in other large-scale grid-connected systems including Fuel Cell (FC), conventional sources such as diesel generator, low inertia Renewable Energy Sources (RES), etc. In addition to that, we will be looking into applying the latest optimization techniques for the SRFCL control strategy.

REFERENCES

[1] S. R. Sinsel, R. L. Riemke, and V. H. Hoffmann, "Challenges and solution technologies for the integration of variable renewable energy sources—A review," *Renew. Energy*, vol. 145, pp. 2271–2285, Jan. 2020.

[2] H. Li and Z. Chen, "Overview of different wind generator systems and their comparisons," *IET Renew. Power Generat.*, vol. 2, no. 2, pp. 123–138, 2008.

[3] B. Sharma, R. Dahiya, and J. Nakka, "Effective grid connected power injection scheme using multilevel inverter based hybrid wind solar energy conversion system," *Electr. Power Syst. Res.*, vol. 171, pp. 1–14, Jun. 2019.

[4] Y. Sawle, S. Gupta, and A. K. Bohre, "PV-wind hybrid system: A review with case study," *Cogent Eng.*, vol. 3, pp. 1–31, Dec. 2016.

[5] L. Wang and M. S.-N. Thi, "Stability enhancement of large-scale integration of wind, solar, and marine-current power generation fed to an SG-based power system through an LCC-HVDC link," *IEEE Trans. Sustain. Energy*, vol. 5, no. 1, pp. 160–170, Jan. 2014.

[6] F. Yang, L. Yang, and X. Ma, "An advanced control strategy of PV system for low-voltage ride-through capability enhancement," *Solar Energy*, vol. 109, pp. 24–35, Nov. 2014.

[7] S. Eftekharnejad, V. Vittal, G. T. Heydt, B. Keel, and J. Loehr, "Impact of increased penetration of photovoltaic generation on power systems," *IEEE Trans. Power Syst.*, vol. 28, no. 2, pp. 893–901, May 2013.

[8] A. M. Howlader and T. Senjyu, "A comprehensive review of low voltage ride through capability strategies for the wind energy conversion systems," *Renew. Sustain. Energy Rev.*, vol. 56, pp. 643–658, Apr. 2016.

[9] M. Mohseni and S. M. Islam, "Review of international grid codes for wind power integration: Diversity, technology and a case for global standard," *Renew. Sustain. Energy Rev.*, vol. 16, no. 6, pp. 3876–3890, 2012.

[10] A. Q. Al-Shetwi, M. Z. Sujod, F. Blaabjerg, and Y. Yang, "Fault ride-through control of grid-connected photovoltaic power plants: A review," *Sol. Energy*, vol. 180, pp. 340–350, Mar. 2019.

[11] A. Q. Al-Shetwi, M. Z. Sujod, and F. Blaabjerg, "Low voltage ride-through capability control for single-stage inverter-based grid-connected photovoltaic power plant," *Solar Energy*, vol. 159, pp. 665–681, Jan. 2018.

[12] O. Noureldeen and A. M. A. Ibrahim, "Low-voltage ride-through capability enhancement of a grid-connected photovoltaic/wind hybrid power system," in *Proc. 19th Int. Middle East Power Syst. Conf. (MEPCON)*, Dec. 2017, pp. 786–795.

[13] A. Movahedi, A. H. Niasar, and G. B. Gharehpetian, "Designing SSSC, TCSC, and STATCOM controllers using AVURPSO, GSA, and GA for transient stability improvement of a multi-machine power system with PV and wind farms," *Int. J. Electr. Power Energy Syst.*, vol. 106, pp. 455–466, Mar. 2019.

[14] M. G. Hemeida, H. Rezk, and M. M. Hamada, "A comprehensive comparison of STATCOM versus SVC-based fuzzy controller for stability improvement of wind farm connected to multi-machine power system," *Electr. Eng.*, vol. 100, no. 2, pp. 935–951, Jun. 2018.

[15] I. Hamdan, A. M. Ibrahim, and O. Noureldeen, "Modified STATCOM control strategy for fault ride-through capability enhancement of grid-connected PV/wind hybrid power system during voltage sag," *Social Netw. Appl. Sci.*, vol. 2, pp. 1–19, Mar. 2020.
[16] M. E. Hossain, "Transient stability improvement analysis among the series fault current limiters for DFIG based wind generator," in *Proc. 19th Int. Conf. Intell. Syst. Appl. Power Syst. (ISAP)*, Sep. 2017, pp. 1–6.
[17] M. Firouzi, M. Nasiri, S. Mobayen, and G. B. Gharehpetian, "Sliding mode controller-based BFCL for fault ride-through performance enhancement of DFIG-based wind turbines," *Complexity*, vol. 2020, pp. 1–12, May 2020.
[18] G. Rashid and M. H. Ali, "Fault ride through capability improvement of DFIG based wind farm by fuzzy logic controlled parallel resonance fault current limiter," *Electr. Power Syst. Res.*, vol. 146, pp. 1–8, May 2017.
[19] M. R. Islam, J. Hasan, M. R. R. Shipon, M. A. H. Sadi, A. Abuhussein, and T. K. Roy, "Neuro fuzzy logic controlled parallel resonance type fault current limiter to improve the fault ride through capability of DFIG based wind farm," *IEEE Access*, vol. 8, pp. 115314–115334, 2020.
[20] M. Firouzi, M. Shafiee, and G. B. Gharehpetian, "Multi-resistor BFCL for FRT capability improvement of DFIG-based wind farm," *IET Energy Syst. Integr.*, vol. 2, no. 4, pp. 316–324, Dec. 2020.
[21] M. Jafari, S. B. Naderi, M. T. Hagh, M. Abapour, and S. H. Hosseini, "Voltage sag compensation of point of common coupling (PCC) using fault current limiter," *IEEE Trans. Power Del.*, vol. 26, no. 4, pp. 2638–2646, Oct. 2011.
[22] *SunPower*. [Online]. Available: http://www.solardesigntool.com/components/module-panel-solar/Sunpower/5915/SPR-305-WHT-D/specification-data-sheet.html
[23] Gamesa. (2010). *Gamesa G80-2.0 MW*. Accessed: Sep. 7, 2010. [Online]. Available: http://www.gamesa corp.com/files/File/G80-ingles.pdf
[24] R. Benadli and A. Sellami, "Sliding mode control of a photovoltaic-wind hybrid system," in *Proc. Int. Conf. Electr. Sci. Technol. Maghreb (CISTEM)*, Nov. 2014, pp. 1–8.
[25] L. Zhu, Q. Li, M. Chen, K. Cao, and Y. Sun, "A simplified mathematical model for power output predicting of building integrated photovoltaic under partial shading conditions," *Energy Convers. Manage.*, vol. 180, pp. 831–843, Jan. 2019.
[26] S. R. Mohamed, P. A. Jeyanthy, D. Devaraj, M. H. Shwehdi, and A. Aldalbahi, "DC-link voltage control of a grid-connected solar photovoltaic system for fault ride-through capability enhancement," *Appl. Sci.*, vol. 9, no. 5, p. 952, Mar. 2019.
[27] W. Kou, D. Wei, P. Zhang, and W. Xiao, "A direct phase-coordinates approach to fault ride through of unbalanced faults in large-scale photovoltaic power systems," *Electr. Power Compon. Syst.*, vol. 43, nos. 8–10, pp. 902–913, Jun. 2015.
[28] S. Alaraifi, A. Moawwad, M. S. El Moursi, and V. Khadkikar, "Voltage booster schemes for fault ride-through enhancement of variable speed wind turbines," *IEEE Trans. Sustain. Energy*, vol. 4, no. 4, pp. 1071–1081, Oct. 2013.
[29] A. F. Tazay, A. M. A. Ibrahim, O. Noureldeen, and I. Hamdan, "Modeling, control, and performance evaluation of grid-tied hybrid PV/wind power generation system: Case study of Gabel El-Zeit region, Egypt," *IEEE Access*, vol. 8, pp. 96528–96542, 2020.
[30] Y. Yang and F. Blaabjerg, "Low-voltage ride-through capability of a single-stage single-phase photovoltaic system connected to the low-voltage grid," *Int. J. Photoenergy*, vol. 2013, pp. 1–10, Feb. 2013.
[31] Y. Bae, T.-K. Vu, and R.-Y. Kim, "Implemental control strategy for grid stabilization of grid-connected PV system based on German grid code in symmetrical low-to-medium voltage network," *IEEE Trans. Energy Convers.*, vol. 28, no. 3, pp. 619–631, Sep. 2013.
[32] Y. Yang, P. Enjeti, F. Blaabjerg, and H. Wang, "Suggested grid code modifications to ensure wide-scale adoption of photovoltaic energy in distributed power generation systems," in *Proc. IEEE Ind. Appl. Soc. Annu. Meeting*, Oct. 2013, pp. 1–8.
[33] A. Q. Al-Shetwi, M. Hannan, K. P. Jern, M. Mansur, and T. Mahlia, "Grid-connected renewable energy sources: Review of the recent integration requirements and control methods," *J. Cleaner Prod.*, vol. 253, pp. 1–17, Apr. 2020.
[34] A. Parida and D. Chatterjee, "Model-based loss minimisation scheme for wind solar hybrid generation system using (grid-connected) doubly fed induction generator," *IET Electr. Power Appl.*, vol. 10, no. 6, pp. 548–559, Jul. 2016.
[35] A. Parida and D. Chatterjee, "An improved control scheme for grid connected doubly fed induction generator considering wind-solar hybrid system," *Int. J. Electr. Power Energy Syst.*, vol. 77, pp. 112–122, May 2016.
[36] J. Mohammadi, S. Vaez-Zadeh, E. Ebrahimzadeh, and F. Blaabjerg, "Combined control method for grid-side converter of doubly fed induction generator-based wind energy conversion systems," *IET Renew. Power Gener.*, vol. 12, no. 8, pp. 943–952, Jun. 2018.
[37] T. R. Ayodele, A.-G. A. Jimoh, J. Munda, and J. Agee, "Dynamic response of a wind farm consisting of doubly-fed induction Generators to network disturbance," in *Proc. Simulation Modeling Methodolog., Technol. Appl.* Berlin, Germany: Springer, 2013, pp. 131–150.
[38] A. Yahiaoui, F. Fodhil, K. Benmansour, M. Tadjine, and N. Cheggaga, "Grey wolf optimizer for optimal design of hybrid renewable energy system PV-diesel generator-battery: Application to the case of Djanet city of Algeria," *Sol. Energy*, vol. 158, pp. 941–951, Dec. 2017.
[39] G. Rashid and M. H. Ali, "Transient stability enhancement of doubly fed induction machine-based wind generator by bridge-type fault current limiter," *IEEE Trans. Energy Convers.*, vol. 30, no. 3, pp. 939–947, Sep. 2015.
[40] A. M. Rauf and V. Khadkikar, "Integrated photovoltaic and dynamic voltage restorer system configuration," *IEEE Trans. Sustain. Energy*, vol. 6, no. 2, pp. 400–410, Apr. 2015.
[41] A. H. Kasem, E. F. El-Saadany, H. H. El-Tamaly, and M. A. A. Wahab, "An improved fault ride-through strategy for doubly fed induction generator-based wind turbines," *IET Renew. Power Gener.*, vol. 2, no. 4, pp. 201–214, Dec. 2008.

AHMED M. A. IBRAHIM was born in Qena, Egypt, in September 1992. He received the Bachelor of Science and Master of Science degrees in electrical engineering from South Valley University, Egypt, in 2014 and 2018, respectively. He worked as an Automation Engineer for two years. He is currently working as a Teaching Assistant with the Faculty of Engineering, South Valley University. His research interests include the integration of renewable energy sources, PV/wind hybrid power systems, and control of the smart grid and micro-grid systems.

I. HAMDAN was born in Qena, Egypt, in 1985. He received the B.Sc. and M.Sc. degrees in industrial electronics and control engineering from the Faculty of Electronic Engineering, Menoufia University, Egypt, in 2008 and 2015, respectively, and the Ph.D. degree from the Department of Electrical Engineering, Faculty of Engineering, South Valley University, Egypt, in 2019. He is currently an Assistant professor with the Department of Electrical Engineering, Faculty of Engineering, South Valley University. His current research interests include control engineering, artificial intelligence, large-scale systems, and renewable energy systems.

SAAD F. AL-GAHTANI (Member, IEEE) received the B.Sc. degree in electrical engineering from King Fahd University of Petroleum and Minerals (KFUPM), Dhahran, Saudi Arabia, in 2011, and the M.Sc. and Ph.D. degrees in electrical engineering from Auburn University, Auburn, Alabama, USA, in 2015 and 2018, respectively. He is currently an Assistant Professor with the Department of Electrical Engineering, College of Engineering, King Khalid University, Abha, Saudi Arabia. His research interests include power electronics, power quality, power systems, and renewable energy.

HANY S. HUSSEIN (Senior Member, IEEE) received the B.Sc. degree in electrical engineering and the M.Sc. degree in communication and electronics from South Valley University, Egypt, in 2004 and 2009, respectively, and the Ph.D. degree in communication and electronics engineering from the Egypt–Japan University of Science and Technology (E–JUST), in 2013. In 2012, he worked as a Special Researcher Student with Kyushu University, Japan. He has been an Associate Professor with the Faculty of Engineering, Aswan University, since 2019. He is currently working as an Assistant Professor with the College of Engineering, King Khalid University, Saudi Arabia. His research interests include digital signal processing for communications, multimedia, image, and video coding, low-power wireless communications, one-bit ADC multiple-input multiple-output, underwater communication, index, and spatial modulation, Li-Fi technology, and visible light communication. He is a Technical Committee Member of many international conferences and a Reviewer of many international conferences, journals, and transactions. Moreover, he was the General Co-Chair of the IEEE ITCE, in 2018.

LOAI S. NASRAT (Member, IEEE) is currently a Professor with the Electrical P&M Department, Faculty of Engineering, Aswan University,. He has been actively involved in both basic and applied research in the area of HV engineering. His research interests include HV insulators, nano polymeric materials, HV cables insulation, aged oil transformer, and environmental studies. He is the author and coauthor of more than 50 papers on nano insulating materials, published in technical journals and proceedings of national and international conferences. He is a member in the Egyptian Sub-Committee of CIGRE and IEC.

MOHAMED A. ISMEIL was born in Qena, Egypt, in October 1977. He received the B.Sc. and M.Sc. degrees in electrical engineering from South Valley University, in 2002 and 2008, respectively, and the Ph.D. degree from Aswan University, in April 2014. From October 2010 to January 2013, he was the Ph.D. Student with the Department of Electrical Drive Systems and Power Electronics, Technical University of Munich, Germany, where he was a Channel System Programmer. From April 2014 to September 2018, he was an Assistance Professor with Aswan Faculty of Engineering, Aswan University. Since October 2018, he has been an Associate Professor with Qena Faculty of Engineering, South Valley University. Since March 2020, he has been the Head of the Electrical Department, Qena Faculty of Engineering. He is currently a member of Aswan Power Electronics Applications Research Center (APEARC). He has published more than 45 papers in international conferences and journals. His main interest is power inverter design for renewable applications. His current research interests include power electronics applications in wind energy conversion system, PV interface with the utility, smart grid technologies, and digital control application (PIC, FPGA, and DSP).